J. Coat. Technol. Res.
DOI 10.1007/s11998-017-9963-0

Numerical investigation of multiple-slot jets in air-knife wiping

A. Yahyaee Soufiani, J. R. McDermid, A. N. Hrymak, F. E. Goodwin

Abstract Gas-jet wiping using an air knife is an effective hydrodynamic method to control the coating thickness of zinc on a moving steel substrate in the continuous hot-dip galvanizing process. The current generation of single-slot air knives is widely used in the galvanizing industry but has limitations in producing low coating weights at the higher line speeds desired for the current generation of automotive sheet steel products. In this work, a novel configuration of a multiple-slot jet (multijet) air knife is investigated through numerical simulations as an alternative to the traditional single-slot air knife. The aim of this study is to investigate the sensitivity of the coating weight to the pressure and shear stress profiles in order to determine whether there are operating regions that are more robust to air-knife geometry changes. A modified geometry for the multislot air knife is proposed based on computational fluid dynamics results obtained from a parametric study. The effects of different operating conditions such as the main jet Reynolds number (Re_m), auxiliary jet Reynolds number (Re_a), and jet-to-wall distances (Z/D) on the final coating thickness were investigated. The results of the modeling showed that by setting the auxiliary jet Reynolds number at a fraction (25%) of the main jet Reynolds number, lighter coating weights can be achieved for higher strip velocities and higher wall-to-jet distances as compared to the single-slot jet design. It is believed that this geometry will provide a robust operating window to enable the prototype design to be employed in the industrial setting.

Keywords Film coating thickness, Multiple-slot jets, Air knives, Continuous hot-dip galvanizing, CFD simulation

List of symbols

C_f	Skin friction coefficient
D_a	Auxiliary jet width (mm)
D	Main jet width (mm)
g	Gravitational acceleration (m/s^2)
G	Nondimensional pressure gradient
h_f	Final film thickness (μm)
p	Static pressure (Pa)
q	Withdrawal flux (1/m^3)
Q	Nondimensional withdrawal flux
Re_a	Auxiliary jet Reynolds number
Re_m	Main jet Reynolds number
s	Auxiliary jet offset (mm)
S	Nondimensional shear stress
u	Fluid velocity (m/s)
V_{strip}	Strip velocity (m/s)
w	Local film thickness (μm)
W	Nondimensional film thickness
Z	Main jet exit-to-wall distance (mm)
μ	Fluid dynamic viscosity (kg/m s)

Presented at the 18th International Coating Science and Technology Symposium, September 19–21, 2016, in Pittsburgh, PA.

A. Yahyaee Soufiani (✉), J. R. McDermid
McMaster University, 1280 Main Street West, Hamilton, ON L8S 4L8, Canada
e-mail: yahyaea@mcmaster.ca

J. R. McDermid
e-mail: mcdermid@mcmaster.ca

A. N. Hrymak
Western University, 1151 Richmond St N, London, ON N6A 5B9, Canada
e-mail: ahrymak@uwo.ca

F. E. Goodwin
International Zinc Association, 2530 Meridian Parkway, Suite 115, Durham, NC 27713, USA
e-mail: fgoodwin@zinc.org

Published online: 27 July 2017

ρ	Fluid density (kg/m^3)
τ	Shear stress (Pa)
θ	Auxiliary jet tilt angle relative to main jet centerline
ρ	Density of gas
R	Universal gas constant (J/mol K)
M_w	Molecular weight of the gas (g/mol)
T	Temperature (K)

Introduction

Continuous hot-dip galvanizing is a coating technique which is widely used in the steel industry. In this process, a steel strip is continuously immersed in a bath of molten liquid zinc, usually at 460°C, during which the liquid metal alloy reactively wets the moving sheet substrate.[1] When the substrate emerges from the bath, it carries out a relatively thick layer of liquid zinc due to viscous drag. The molten zinc coating thickness on the sheet substrate is usually controlled just above the bath through the use of a planar turbulent gas jet or air knife, typically in a single-slot configuration (Fig. 1). The pressure gradient and shear stress applied to the liquid film by the jet control the film thickness above the air knife, and the majority of the liquid returns to the bath as a runback flow.[2–5] The film thickness after wiping (h_f) depends on the substrate velocity V_{strip}, the nozzle pressure P_0, the nozzle-to-substrate standoff distance Z, the nozzle slot width D, and the physical properties of the liquid zinc.[6,7] In industry, the general ranges of $0.8 \leq D \leq 1.5$, $8 \leq Z/D \leq 12$ and $5000 \leq Re \leq 25{,}000$ are commonly used.

Thornton and Graff[2] proposed a model for calculating the final liquid film thickness by assuming that the reduction of film thickness was due solely to the pressure gradient created by the impinging jet. Tuck[3] used a similar approach and checked the stability of the solutions for long-wavelength perturbations. Ellen and Tu[4] subsequently incorporated the effect of wall shear stress distribution into the coating weight model. Tu and Wood[6] experimentally measured the wall pressure and shear stress distribution beneath an impinging jet for a wide range of plate-to-nozzle ratios of $2 < Z/D < 20$ and Reynolds numbers $3000 \leq Re_m \leq 11{,}000$. Guo and Wood[8] measured the wall shear stress for a jet with a free stream turbulence intensity of approximately 0.35% at the jet exit. They compared their results with Tu and Wood,[6] where their turbulence level was approximately 4%. By comparing these results, they concluded that the turbulence intensity had only a second-order influence on the wall shear stress within the jet stagnation region.

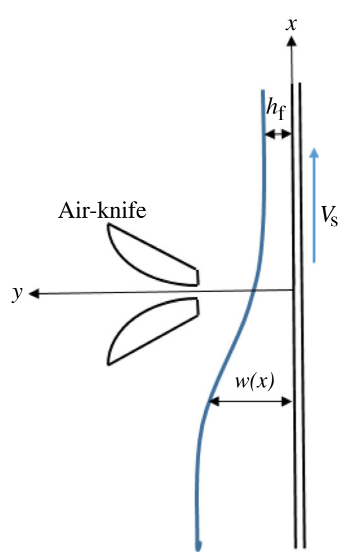

Fig. 1: Schematic of the gas-jet wiping process

Naphade et al.[9] proposed a model to estimate the coating weight as a function of strip velocity, jet nozzle pressure, plate-to-nozzle distance, and nozzle gap width. The proposed correlation was validated with industrial line data. Gosset et al.[7] presented a model to predict the gas-jet wiping performance at small standoff distances and showed that the final coating thickness did not change significantly for $Z/D < 7$ for a given jet velocity. Elsaadawy et al.[10] developed a coating weight model as a function of operating parameters for $Z/D \leq 8$. By combining experimental and computational methods, they improved the pressure and shear stress correlations using the $k - \varepsilon$ turbulence model in the FLUENT code. The model showed good agreement with industrial data, particularly at lower coating weights, where the maximum deviation was 8% between the predicted coating weight and measured data. Lacanette et al.[11] used a LES turbulence model in order to obtain the mean pressure gradient and shear stress distribution induced by a single-slot jet on a dry wall. The obtained profiles were then applied in a knife model. The authors also used VOF method coupled with LES model in order to study the effect of turbulent jet on a moving wall containing a layer of liquid film. By comparing the decoupled lubrication model and the two-phase model, they concluded that the knife model is demonstrated to be a good estimator for the final film thickness.

In order to obtain lighter coating weights at reasonable strip velocities, the usual practice would be to increase the wiping pressure (i.e., increase the jet velocity) significantly. However, increasing the wiping pressure can result in increased noise, an industrial hygiene issue, or splashing. Splashing is characterized by the ejection of zinc droplets from the strip which can be deposited on or around the jet nozzle or on the strip itself, resulting in defects. Dubois[12] showed that full splashing occurs for a zinc coating thickness of 20 μm produced at line speeds of 160–170 m/min when $Z/D < 6$. Splashing is initiated at the edge of the strip and spreads toward the center of the strip. Therefore, full splashing occurs throughout the whole sheet width and makes the running back flow to detach from the substrate and causes defects on the final product. Kim et al.[13] proposed a multiple-slot air-knife design which comprised a main jet and four inclined auxiliary jets discharging air at lower velocity in comparison with the main slot jet. In this design, the gas discharging from the main and auxiliary jets provided the necessary force for wiping the excess molten zinc from the sheet. It was claimed that the second auxiliary jets prevented splashing where the auxiliary jets restrained zinc droplets from splashing by mixing the gas particles of the main jet and lower speed auxiliary jets such that the wall shear stress was reduced, thereby preventing splashing.

In this study, a novel multijet configuration based on the proposal of Kim et al.[13] was studied through numerical simulations as the zinc wiping apparatus in the continuous hot-dip galvanizing (CHDG) process. In particular, the objective of this paper is to investigate the sensitivity of the coating weight to the pressure and shear stress profiles to determine whether there are operating regions that are robust to the prototype air knife operating parameter changes and to also determine whether lower coating weights at high line speeds can be obtained through the use of the proposed multislot air knife.

Analytical model of film thickness

Calculation of the liquid zinc volumetric flux on the steel strip, q, is the first step in the modeling of coating thickness.[10] A condensed summary of the analysis is provided below to demonstrate the assumptions applied to calculating the thickness of the liquid film. A simplified form of the Navier–Stokes equation can be used for calculating q based on the assumptions of steady-state, isothermal, incompressible flow of the liquid film, where it is assumed that surface tension can be neglected and that the no-slip condition of the liquid on the steel strip is valid.[4] Fluid properties, such as viscosity and density, were assumed to be constant. By considering the above assumptions, the two-dimensional Navier–Stokes equation for a thin film on a flat plate reduces to:

$$\mu\frac{d^2u}{dy^2}-(\rho g+\frac{dp}{dx})=0 \tag{1}$$

Using the coordinate system in Fig. 1, the boundary conditions can be written as:

$$u=V_s \quad \text{at } y=0 \tag{2}$$

$$\mu\left(\frac{\partial u}{\partial y}\right)=\tau \quad \text{at } y=w \tag{3}$$

where τ is the shear stress imposed by the turbulent impinging slot jet on the strip, V_{strip} is the strip velocity, and w is the local film thickness. Integrating equation (1) and applying the boundary conditions in equations (2) and (3) yields:

$$u=V_s\left[1+\frac{y}{w}SW-\frac{y}{w}\left(2-\frac{y}{w}\right)\frac{GW^2}{2}\right] \tag{4}$$

where $W=w\sqrt{\frac{\rho g}{\mu V_s}}$ is the nondimensional film thickness, $S=\frac{\tau}{\sqrt{\rho\mu V_s g}}$ is the nondimensional shear stress, and $G=1+\frac{1}{\rho g}\frac{dp}{dx}$ is the effective gravitational acceleration. The liquid volumetric flux, q, can then be calculated as:

$$q=\int_0^w u\,dy=V_s w\left(1+\frac{SW}{2}-\frac{GW^2}{3}\right) \tag{5}$$

The nondimensional withdrawal flux, $Q=\frac{q}{V_S}\sqrt{\frac{\rho g}{\mu V_S}}$, can be derived from equation (5) by substitution and rearrangement as:

$$Q=-\frac{GW^3}{3}+\frac{SW^2}{2}+W \tag{6}$$

From Elsaadawy et al.,[10] the nondimensional film thickness W, corresponding to the maximum withdrawal flux, Q_{max}, can be determined by solving $\frac{dQ}{dW}=0$ and employing the quadratic formula such that:

$$W=\frac{S\pm\sqrt{S^2+4G}}{2G} \tag{7}$$

Using the above formalism, the nondimensional film thickness is a function of dp/dx and τ at any coordinate x. Due to mass continuity, the minimum value of Q_{max} corresponding to every x value is the physically available withdrawal flux, Q. The final film velocity is assumed equal to the substrate velocity and the final coating thickness, h_f, is given by

$$h_f=\frac{q}{V_S}=\frac{(Q_{max})_{min}}{\sqrt{\frac{\rho g}{\mu V_S}}} \tag{8}$$

The distribution of shear stress and pressure gradient along the wall can be used in equations (7) and (8) to estimate the final coating thickness on a moving substrate. Higher values for the dp/dx and τ distributions in the vicinity of wiping region can lead to a lower coating thickness according to equations (6) through (8). In this study, the pressure gradient and shear stress distributions induced by both the single and multiple jet geometries on a dry, fixed surface were determined through numerical simulations.

Numerical modeling

A computational approach was used to model the pressure distribution and shear stress on the wall. The computations were carried out using FLUENT 14.0 commercial software. The solver was pressure based, and all of the simulations were run in steady mode. The SIMPLE method was used for pressure–velocity coupling. Fluid flow can be represented by the Navier–Stokes equations which contain the mass and momentum balance equations. In Cartesian form, they are as follows:

$$\frac{\partial \rho}{\partial t} + \frac{\partial(\rho u_i)}{\partial x_i} = 0 \tag{9}$$

$$\frac{\partial \rho u_i}{\partial t} + \frac{\partial \rho u_i u_j}{\partial x_i} = -\frac{\partial p}{\partial x_i} + \frac{\partial}{\partial x_i}\left[\left(\frac{\partial u_i}{\partial x_j} + \frac{\partial u_j}{\partial x_i}\right)\right] \tag{10}$$

The well-known two-equation model was used to capture turbulence properties. One of the transport equations solved for the turbulent kinetic energy (k) and the other solved for the turbulent dissipation rate (ε). The turbulence model which was used in this study for all cases was the standard ($k - \varepsilon$) model, which includes the following two equations:

$$\frac{\partial \rho k}{\partial t} + \frac{\partial \rho k u_i}{\partial x_i} = \frac{\partial}{\partial x_j}\left[\left(\mu + \frac{\mu_t}{\sigma_k}\right)\frac{\partial k}{\partial x_j}\right] + G_k - \rho\varepsilon \tag{11}$$

$$\frac{\partial \rho \varepsilon}{\partial t} + \frac{\partial \rho \varepsilon u_i}{\partial x_i} = \frac{\partial}{\partial x_j}\left[\left(\mu + \frac{\mu_t}{\sigma_\varepsilon}\right)\frac{\partial \varepsilon}{\partial x_j}\right] + C_{1\varepsilon}\frac{\varepsilon}{k}(G_k) - C_{2\varepsilon}\rho\frac{\varepsilon^2}{k} \tag{12}$$

where the turbulent viscosity for the standard k-ε turbulence model is written as:

Table 1: Standard k–ε turbulence model constants

C_μ	$C_{1\varepsilon}$	$C_{2\varepsilon}$	σ_k	σ_ε
0.09	1.44	1.92	1	1.3

$$\mu_t = \rho C_\mu k^2 / \varepsilon \tag{13}$$

where C_μ is a model constant. Table 1 provides the standard k-ε model constants for equations (11) through (13) from Launder and Sharma.[14]

A double precision solver was used for all simulations. A segregated solver was used for the governing equations. The standard method was used for the pressure term with a first-order up-winding scheme for the turbulent kinetic energy (k), turbulent dissipation rate (ε), and momentum. The governing equations were solved until the root-mean-square (RMS) residuals for all governing equations fell below 10^{-6}. A constant viscosity for the air was assumed, and the air density was computed as a function of pressure and temperature based on the ideal gas law:

$$\rho = \frac{P}{\frac{R}{\mu_w} T} \tag{14}$$

Boundary conditions and grid generation

Schematics of the two nozzle geometries are illustrated in Fig. 2. For the initial numerical simulations and for validation purpose, the auxiliary jet width (D_a), distance between the exit of the main and auxiliary jets (s), and the main jet slot width (D) were fixed at 3, 20, and 1.5 mm, respectively. The inclination of the auxiliary jets relative to the main jet centerline was 20°. The boundary conditions were the no-slip condition at the impingement and nozzle walls, a pressure inlet at the nozzle inlets, and a pressure outlet at the exit of the computational domain. The mesh used for the impinging jets comprised a mixture of quadrilaterals and triangles. The full physical domain was solved, not taking into account geometric symmetry. Grid cluster-

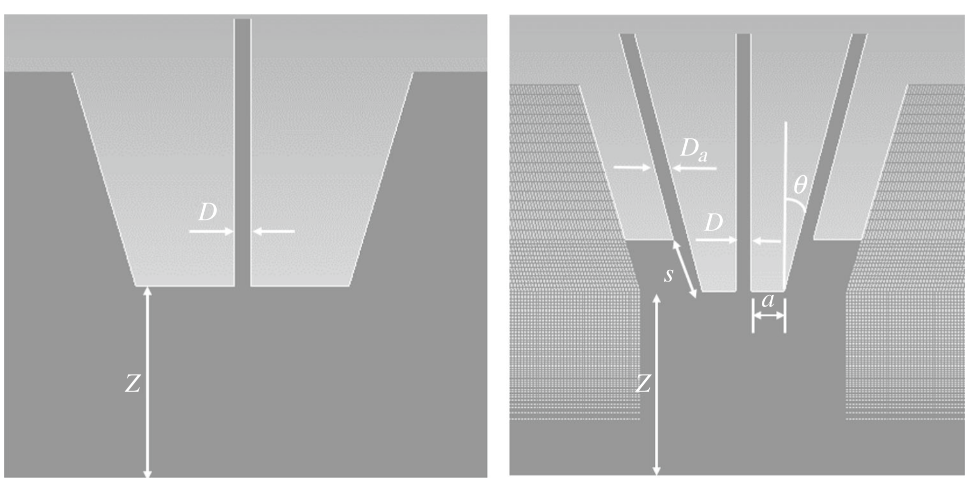

Fig. 2: Schematic of the single-slot jet and multiple-slot jet geometries used (D_a = 1.5 mm, s = 20 mm, D = 1.5 mm, θ = 20°, a = 3 mm)

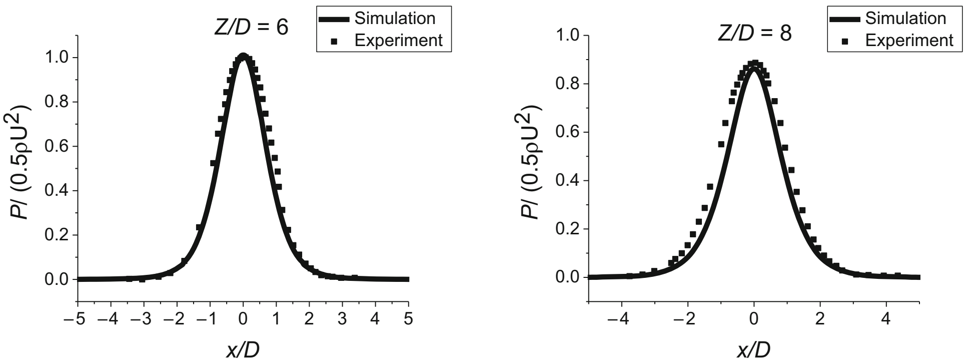

(a) (b)

Fig. 3: Comparison of numerical pressure distribution and pressure gradient vs the experimental measurements of Alibeigi[15] for a single-slot jet

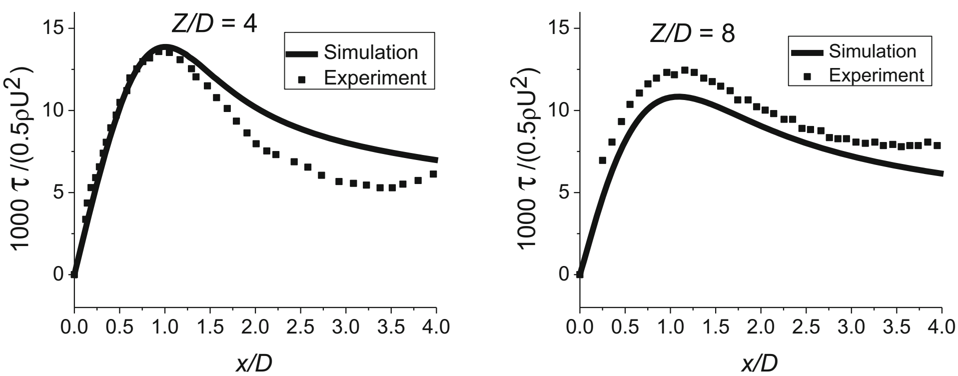

(a) (b)

Fig. 4: Comparison of wall shear stress profiles predicted by numerical simulations vs the experimental measurements of Ritcey[16] for a single-slot jet for *Z*/*D* = 4 and *Z*/*D* = 8

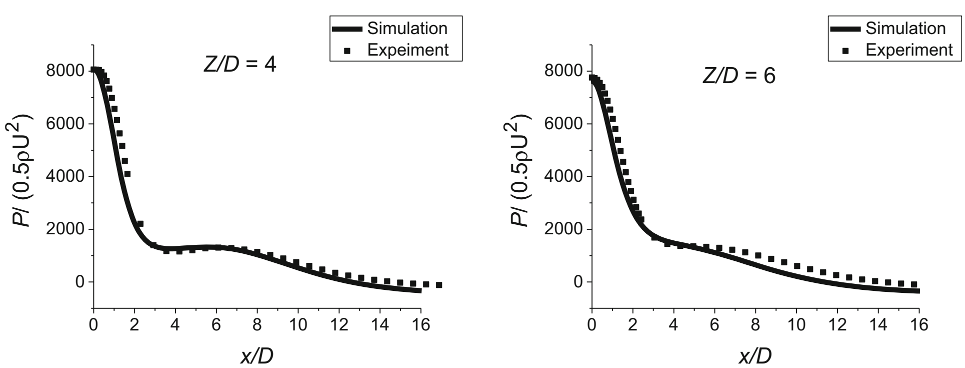

(a) (b)

Fig. 5: Comparison of numerically predicted wall pressure distribution vs the experimental measurements of Alibeigi[15] for the multislot jet geometry where $D = 1.5$ mm, $D_a = 3$ mm, and $s = 19.7$ mm

ing was used adjacent to the wall and around the centerline where large gradients in the velocity field, pressure field, and turbulent parameters were present. Four grids with differing numbers of nodal points were tested to verify mesh independence of the numerical results. In order to capture the severe pressure gradients and rapid changes of flow in the near-wall region, the mesh was refined such that the first node located in

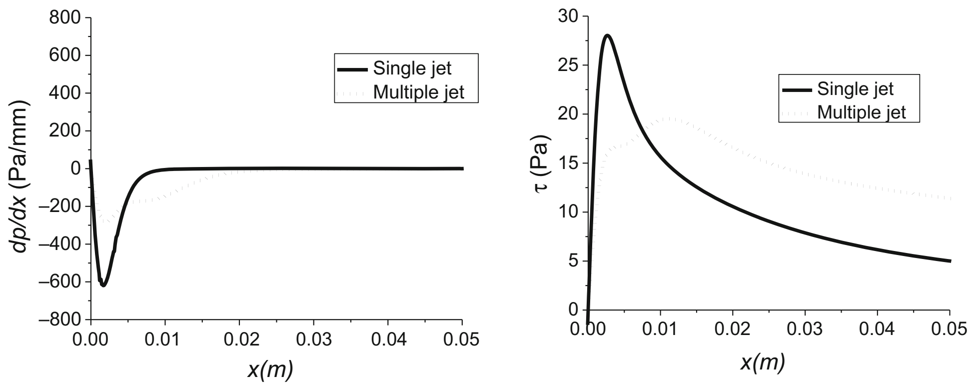

Fig. 6: Comparison of numerical results for the pressure gradient and wall shear stress for the single- and multislot air-knife geometries where $Re_m = Re_a$ = 11,000, D = 2.5 mm, D_a = 3 mm, s = 19.7 mm, and θ = 20° for Z/D = 8

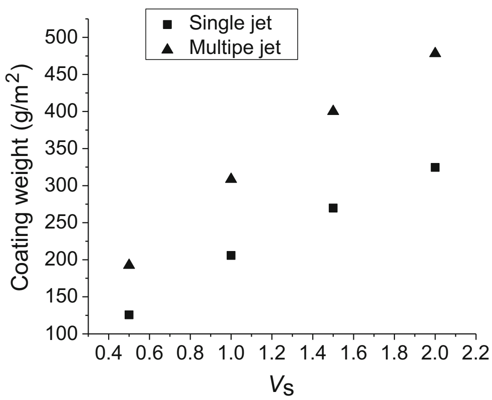

Fig. 7: Coating weight as a function of strip velocity for the single- and multislot jet air knives for Re_m = 11,000, Re_a = 11,000, and Z/D = 8

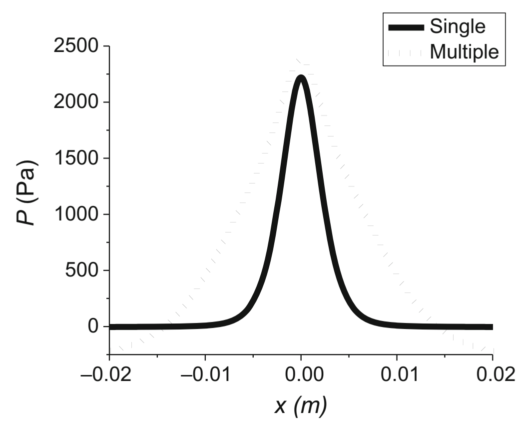

Fig. 8: Comparison of the typical pressure profiles for the single- and multiple-slot jets for Re_m = 11,000, Re_a = 11,000, and Z/D = 8

the viscous sub-layer ($y^+ \sim 1$) and the mesh size near the wall is approximately 4 μm. The computational domain size was $L/D = -85$ to $L/D = 85$.

Validation

Numerical simulations vs experimental wall pressure distribution and pressure gradient data for different wall-to-jet distances at Re_m = 11,000 are presented in this section. Figure 3 presents a comparison of numerical nondimensional wall pressure profiles vs the experimental data of Alibeigi[15] for a short nozzle single-slot planar impinging jet as function of Z/D. It can be seen that the value of the predicted maximum nondimensional pressure and pressure distribution was in good agreement with the experimental data. Figure 4 compares the numerical and experimental results for the wall skin friction $C_f = \tau_w / (0.5 \rho U^2)$. From this, it can be seen that the numerical skin friction results compare very well with the corresponding experimental measurements of Ritcey.[16] It can also be seen that the maximum C_f value decreased with increasing Z/D. The decreasing skin friction can be attributed to the decaying velocity of the jet and momentum losses due to fluid entrainment. Figure 5 shows a comparison of the numerical wall pressure profile vs the experimental data of Alibeigi[15] for the multislot impinging jet where $Re_m = Re_a$ = 11,000. From Fig. 5, it can be seen that the numerical models of the multislot jet geometry also agree well with the experimental measurements. From the above, it can be concluded that the numerical models for both the single- and multislot geometries have been experimentally verified.

Results and discussion

Figure 6 illustrates the wall pressure gradient and wall shear stress distribution for both the single- and multiple-slot air-knife geometries. According to this figure, lower values of the pressure gradient and shear stress are distributed in the vicinity of the wiping point for the multislot air-knife design. This leads to a higher coating liquid flow rate Q from the bath which remains on the substrate after wiping, as described by equation (6). Accordingly, in Fig. 7, which shows the variation of coating weight as a function of strip velocities between 0.5 m/s and 2.5 m/s, the single-slot air knife has a better performance in terms of coating weight reduction vs the examined configuration of multislot air knife. The same results were obtained for a wide range of operating conditions.

By comparing the wall pressure profiles for the two air-knife geometries, as shown in Fig. 8, it can be seen that the auxiliary jets not only increased the maximum impingement pressure, but they can broaden the pressure distribution along the wall, resulting in a lowering of the pressure gradient (dp/dx) distribution.

Subsequent simulations investigated the effects of changing various geometric parameters such as D_a, a, s, and θ per Fig. 2 in order to modify the multislot air-knife geometry such that the pressure profile and pressure gradient conformed more closely to the single-slot air-knife shape without losses in (dp/dx), the results of which are discussed in the following sections.

Effect of D_a

The effect of the auxiliary jet gap, D_a, on the wall pressure distribution was studied numerically. The main slot jet Reynolds number was fixed at 11,000, which corresponds to an air velocity of 110 m/s. Three different values of D_a = 1.5, 2, and 3 mm were examined while a and s were fixed at 3 mm and 5 mm, respectively.

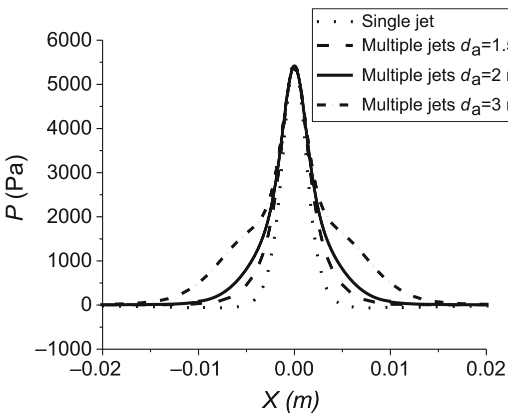

Fig. 9: Effect of D_a on wall pressure profile for Z/D = 8, Re_m = 11,000, Re_a = 6000, a = 3 mm, and s = 5 mm

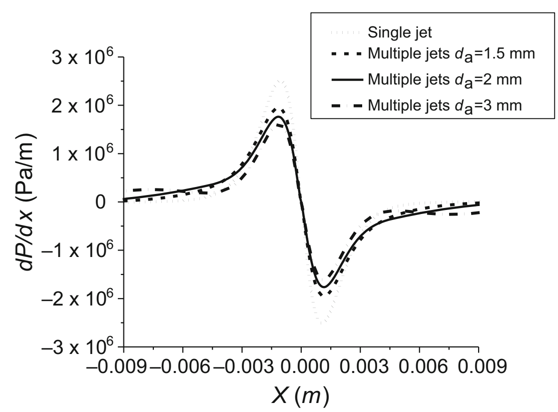

Fig. 11: Effect of D_a on wall pressure gradient for Z/D = 8, Re_m = 11,000, Re_a = 6000, a = 3 mm, and s = 5 mm

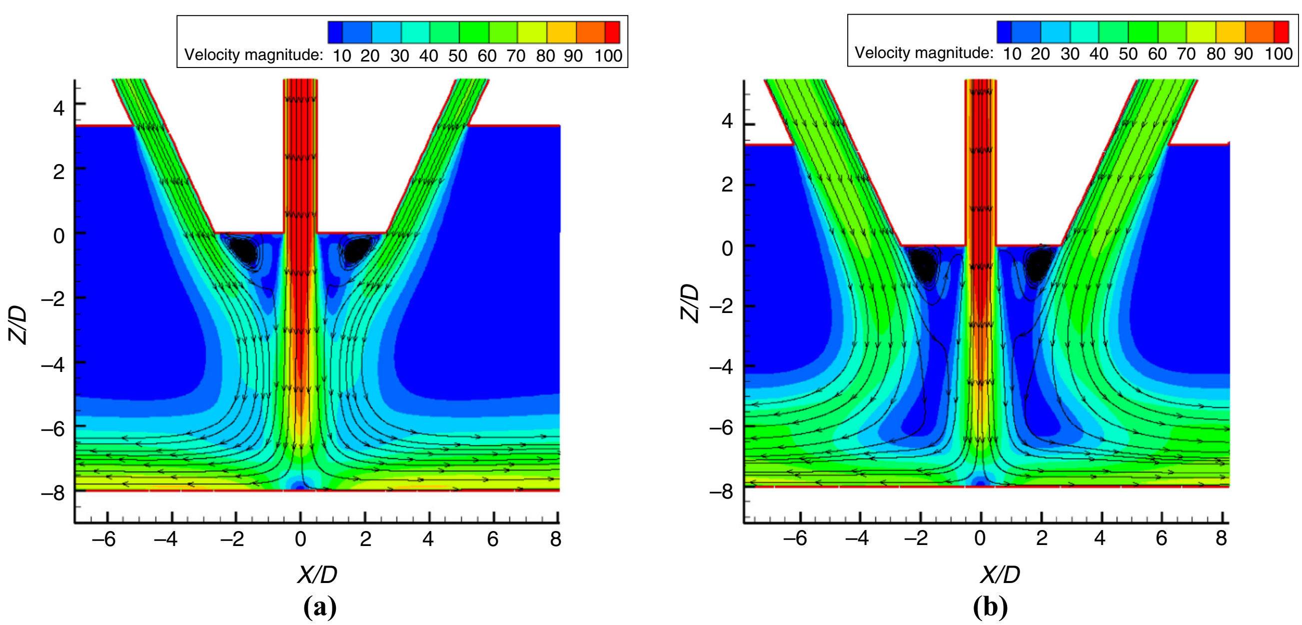

Fig. 10: Velocity contour and streamlines with Z/D = 8, Re_m = 11,000, Re_a = 6000, a = 3 mm, and s = 5 mm for (a) D_a = 1.5 mm and (b) D_a = 3 mm

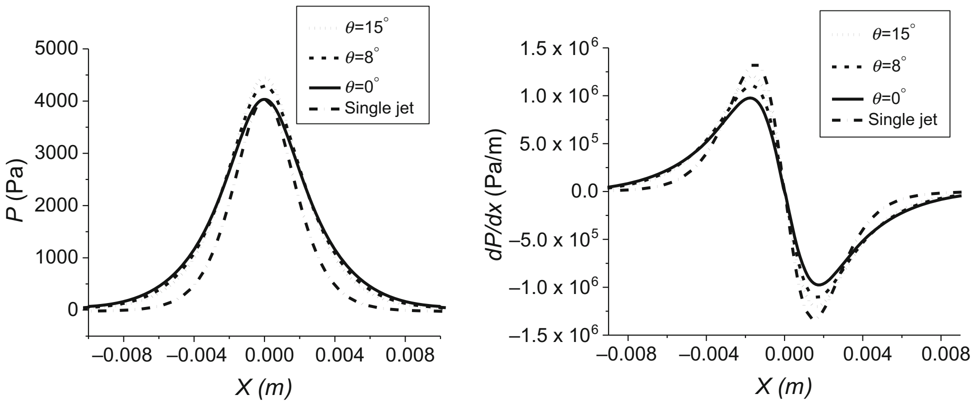

Fig. 12: Effect of θ on wall pressure profile and wall pressure gradient for Z/D = 12, Re_m = 11,000, Re_a = 6000, a = 3 mm, s = 5 mm, and $D = D_a$ = 1.5 mm

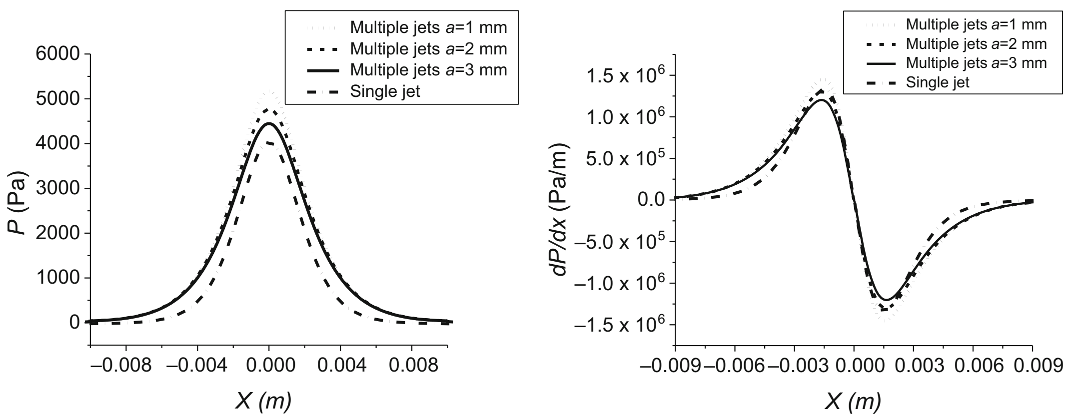

(a) (b)

Fig. 13: Effect of a on wall pressure profile and wall pressure gradient for Z/D = 12, Re_m = 11,000, Re_a = 6000, s = 5 mm, and $D = D_a$ = 1.5 mm

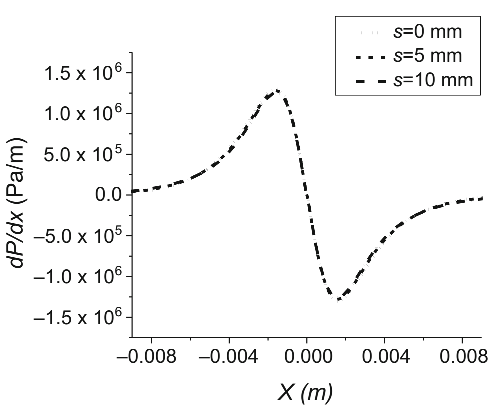

Fig. 14: Effect of s on the wall pressure gradient for Z/D = 12, Re_m = 11,000, Re_a = 6000, a = 2 mm, and $D = D_a$ = 1.5 mm

Figure 9 shows the wall pressure distribution as a function of the auxiliary jet gap width, D_a, where Z/D, Re_m, Re_a, a, and s were held constant as documented in the figure caption. It can be seen that adding auxiliary jets to the main jet changed the wall pressure profile distribution as compared to the single-slot impinging jet wall pressure. The secondary peak that was observed for higher D_a values disappeared by decreasing D_a and pressure profile became sharper. According to Fig. 10, for high D_a values, the auxiliary jet flow could not be merged effectively with the main jet flow in the vicinity of the wiping region. Instead, the auxiliary nozzles gas particles, which have the lower speed compared to the main nozzle, collide with the main jet gas particles downstream of the impinging point and it results in the overall gas speed decrease along the length of the steel substrate. However, for lower D_a the streamlines of the auxiliary jet merged with the main jet flow, and therefore, more momentum has been added in vicinity of the main jet centerline. This leads to a higher pressure gradient in the impingement region.

Figure 11 illustrates the wall pressure gradient for the pressure profiles presented in Fig. 9. According to this figure, the pressure gradient distribution in the

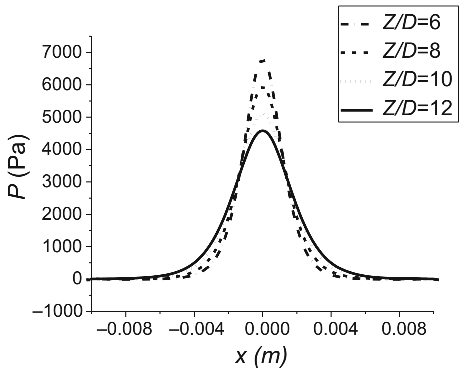

Fig. 15: Wall pressure distribution of the modified multi-slot air knives for different *Z/D*, where Re_m = 11,000 and Re_a = 3000 for D_a = 1.5 mm *D* = 1.5 mm, *a* = 1 mm, *s* = 0

vicinity of the wiping region remained significantly higher for the single-slot jet relative to the multislot air knife. From this result, the multislot air-knife geometry needs to be modified in order to obtain a thinner coating when using the multiple jet design.

Effect of auxiliary jet tilt angle (θ)

In this section, the effect of the auxiliary jet tilt angle (θ) on the wall pressure distribution and wall pressure gradient was investigated. The main and auxiliary jet Reynolds numbers were fixed at Re_m = 11,000 and Re_a = 6000, respectively, and $D = D_a = 1.5$ mm, $a = 3$ mm, $s = 5$ mm, and $Z/D = 12$. The main jet was perpendicular to the impingement plate, and the

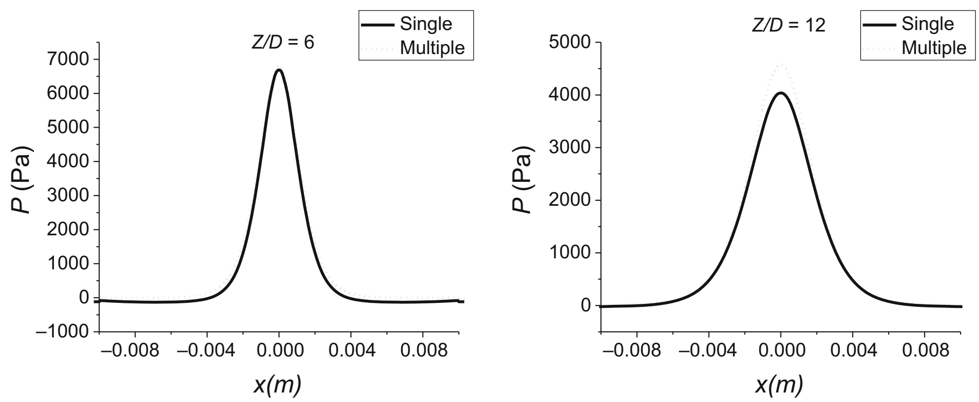

Fig. 16: Comparison of wall pressure distribution for *Z/D* = 6 and *Z/D* = 12, where Re_m = 11,000 and Re_a = 3000 for D_a = 1.5 mm *D* = 1.5 mm, *a* = 1 mm, *s* = 0

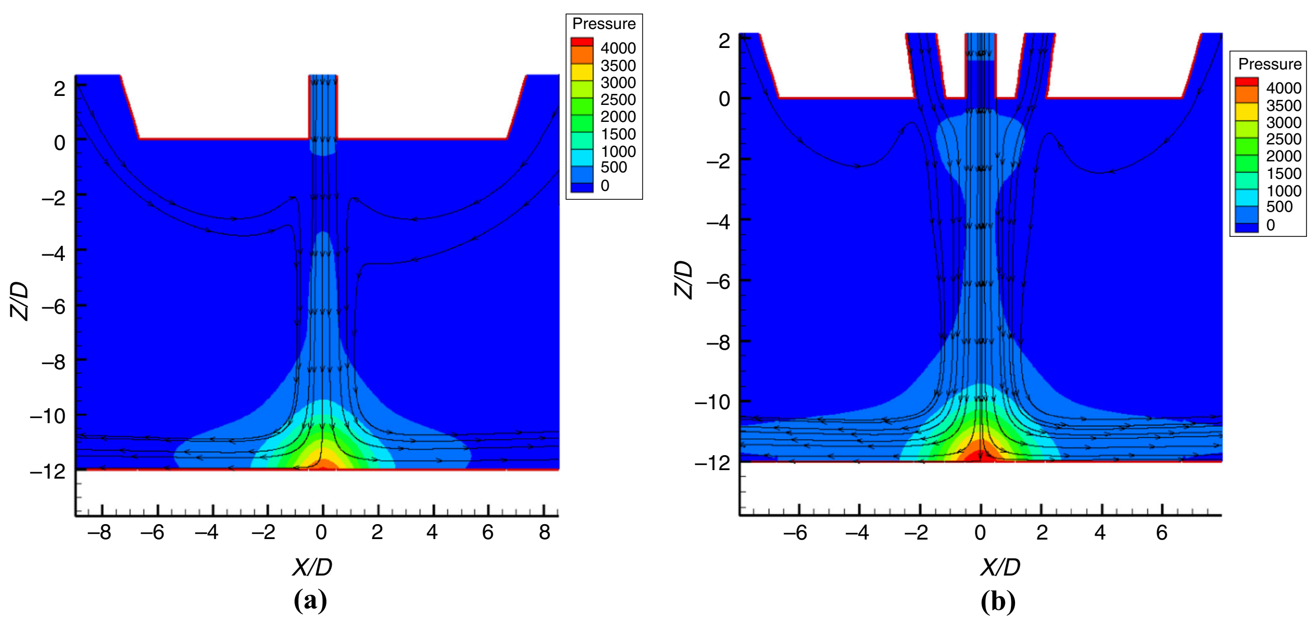

Fig. 17: Pressure contour and streamlines for *Z/D* = 12, for (a) single-slot jet, (b) multislot jets where Re_m = 11,000 and Re_a = 3000 for D_a = 1.5 mm *D* = 1.5 mm, *a* = 1 mm, *s* = 0

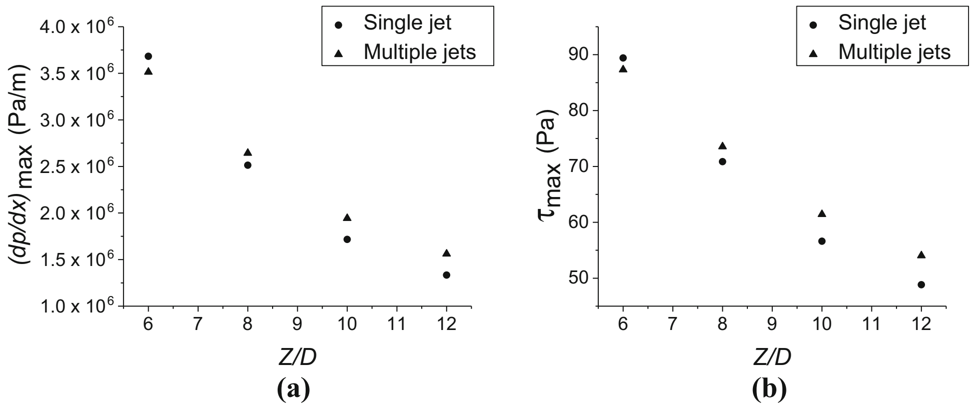

Fig. 18: Comparison of maximum (a) wall pressure gradient and (b) shear stress for different *Z/D* ratios for D_a = 1.5 mm D = 1.5 mm, a = 1 mm, s = 0

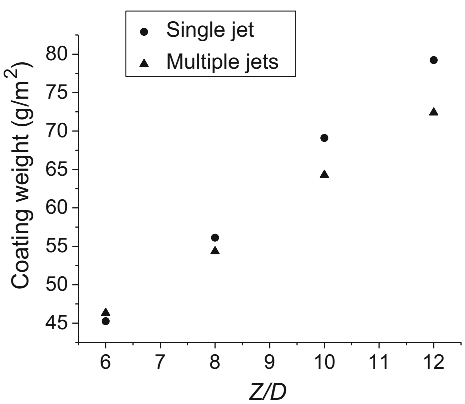

Fig. 19: Comparison of coating weight for a single-slot jet and modified multiple-slot jets for different *Z/D* ratios, with V_{strip} = 0.5 m/s, Re_m = 11,000 and Re_a = 3000, for D_a = 1.5 mm D = 1.5 mm, a = 1 mm, s = 0

auxiliary jets were inclined at $\theta = 0°$, 8°, and 15° relative to the main jet centerline as defined in Fig. 2 (please recall that $\theta = 20°$ in the computations documented above). In order to compare the results, mesh was reset to keep similar refinement near the wall and jet centerlines for each of the case studies. Figure 12 shows the resultant wall pressure distributions and wall pressure gradients for the various θ documented above.

According to Fig. 12a, the maximum pressure value was sensitive to the auxiliary jet tilt angle and, by inclining the auxiliary jet toward the main jet centerline, a higher maximum pressure could be achieved. For $Z/D = 12$ and $a = 3$ mm, the highest maximum pressure and maximum pressure gradient distribution were obtained for $\theta = 15°$ in which the main and auxiliary jet centerlines were coincident at a same point on the impingement wall. In this arrangement for the multislot air knife, the auxiliary jet flows merged with the main jet flow and formed a single flow field. Thus, the additional momentum from the auxiliary jets aided in increasing the main jet flow field momentum and a higher $(dp/dx)_{max}$ could be achieved, as is shown in Fig. 12b. However, it can also be seen that the maximum pressure gradient value continued to be lower for the multislot air-knife design as compared to the single-slot jet under these operating conditions.

Effect of a

Figure 13 illustrates the effect of main jet-to-auxiliary jet distance (*a*, Fig. 2) on the wall pressure profile and wall pressure gradient. The main and auxiliary jet Reynolds numbers were fixed at Re_m = 11,000 and Re_a = 6000, respectively, the jet-to-wall distance was fixed at Z/D = 12, and "*a*" varied between a = 1 mm and a = 3 mm while s and D_a were fixed at 5 mm and 1.5 mm, respectively, where θ was varied between 8° and 15° in a way that the jet centerlines were coincident at a same point on the wall.

It was observed that by decreasing the distance between the main jet and auxiliary jets (*a*), a higher maximum pressure value could be achieved while increasing the pressure profile gradient. Consequently, in Fig. 13, the pressure gradient distribution increased by decreasing "*a*" and, for a = 1 mm, the multislot air knives had a higher $(dp/dx)_{max}$ as compared to the single-slot jet.

Effect of s

In this section, the effect of the auxiliary jet offset (*s*, Fig. 2) on the wall pressure gradient and wall shear stress profiles was investigated. The main and auxiliary jet Reynolds numbers were fixed at Re_m = 11,000 and Re_a = 6000, respectively, and the jet-to-wall distance was fixed at Z/D = 12, a = 2 mm, $D = D_a$ = 1.5 mm, and s ranged between 0 mm to 10 mm. According to Fig. 14, there was no significant effect on the pressure gradient profiles for the range of s values investigated.

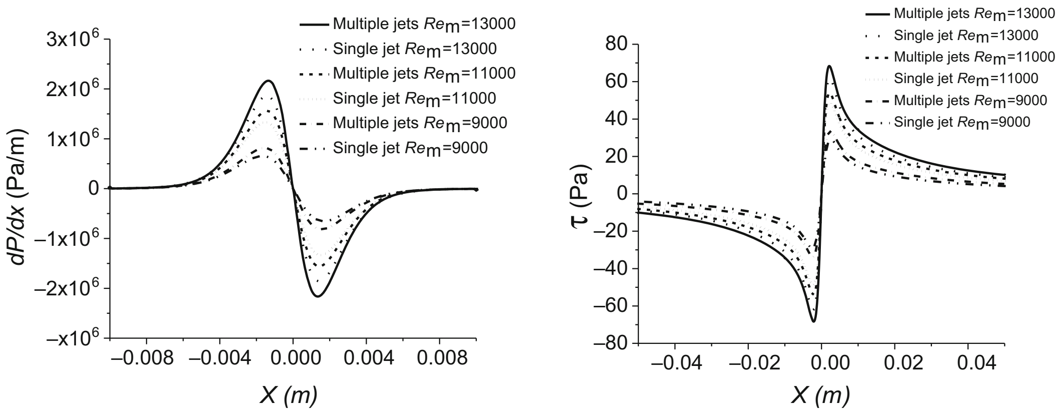

Fig. 20: Effect of main jet Reynolds number on pressure gradient and shear stress distribution of the modified multiple-slot jets for Z/D = 12, Re_a = 3000, D_a = 1.5 mm D = 1.5 mm, a = 1 mm, s = 0, θ = 8°

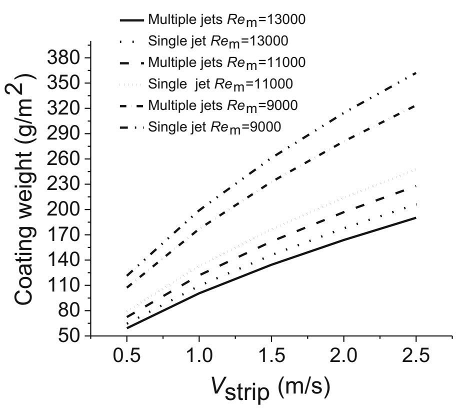

Fig. 21: Coating weight of the single-slot jet and modified multislot jet for various Re_m and V_{strip} with Z/D = 12 and Re_a = 3000, D_a = 1.5 mm D = 1.5 mm, a = 1 mm, s = 0, θ = 8°

Based on the above numerical simulation results, the dimensions for the multiple-slot air knives were modified such that $D = D_a = 1.5$ mm, $a = 1$ mm, $s = 0$, and θ varied between 8° and 16° for various Z/D ratios to facilitate convergence of the main and auxiliary jets at the wall along the centerline of the main jet.

Effect of jet-to-wall distance

According to Dubois,[12] coating thickness reduction through gas-jet wiping strongly depends on the nozzle-to-strip distance in the range of line speeds of over 100 m/min and $Z/D \geq 7$. In this section, the effect of Z/D on the wall pressure gradient and shear stress distribution for the modified multislot air-knife design was investigated and their resultant coating weights on a moving substrate computed. Results of the flow field and coating weight for the modified multislot air knife were compared with the results of the traditional single-slot jet air knife. In the modified design, for each specific Z/D, θ was set in a way that all three jet centerlines converged on the wall at the centerline of the main jet.

Figure 15 illustrates the wall pressure distribution for different values of Z/D for Re_m = 11,000 and Re_a = 3000. It can be seen that the maximum pressure decreased significantly with increasing Z/D. Moreover, by comparing wall pressure distribution for the single jet and multislot jets in Fig. 16, it can be seen that for high Z/D ratios, higher maximum pressure can be obtained for the multislot jets. This can be explained by the pressure contour and streamlines in Fig. 17. According to this figure, the flow from the auxiliary combines with the main jet flow and increases its momentum. This increment can compensate for some part of the jet momentum loss due to locating of the wall outside the jet potential core. Therefore, higher stagnation pressure was observed for the multislot jets compared to the single jet. However, this trend was not seen for low Z/D = 6 where the impingement wall was already located within the potential core.

Figure 18 illustrates the maximum wall pressure gradient and shear stress for different Z/D ratios for both the single-slot jet and modified version of the multijet geometry for Re_m = 11,000 and Re_a = 3000, $D_a = D$=1.5 mm, a = 1 mm and s = 0. It is shown in this Figure that the nondimensional maximum wall pressure gradient for the multiple-slot jets was higher compared to the single-slot jet for $Z/D \geq 8$ and decreased continuously with increasing Z/D where the largest difference between the two configurations was approximately 18% for Z/D = 12.

Figure 18b compares the maximum wall shear stress at Re_m = 11,000 and Re_a = 3000. For both configurations, the maximum wall shear stress decreased with increasing Z/D ratio, where the rate of shear stress decrement for the single-slot jet geometry was higher than for the modified multislot design. The value of the maximum shear stress was higher for the single jet geometry for $Z/D \geq 8$. The largest difference between

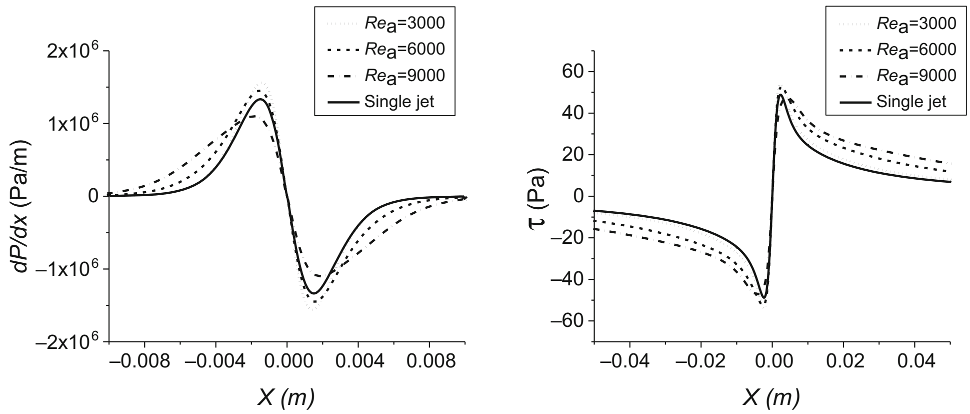

Fig. 22: Effect of auxiliary jet Reynolds number on wall pressure gradient and wall shear stress for the modified multislot jet with Re_m = 11,000 and Z/D = 12, D_a = 1.5 mm D = 1.5 mm, a = 1 mm, s = 0, θ = 8°

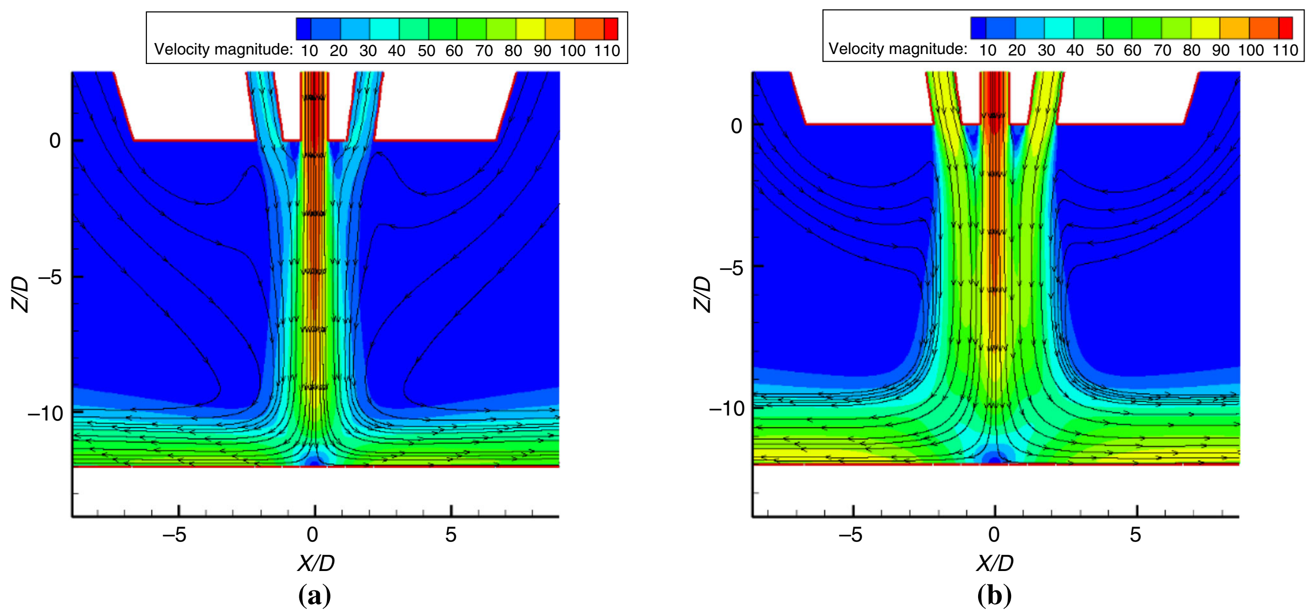

Fig. 23: Pressure contour and streamlines for (a) Re_a = 3000 and (b) Re_a = 9000 where Z/D = 12, Re_m = 11,000, D_a = 1.5 mm D = 1.5 mm, a = 1 mm, s = 0

the maximum wall shear stress was approximately 11% for $Z/D = 12$.

Figure 19 shows a comparison of the coating weights for a single jet and the modified multislot jet as a function of Z/D ratio with $V_{strip} = 0.5$ m/s, $Re_m = 11{,}000$, $Re_a = 3000$, $D = D_a = 1.5$ mm, $a = 1$ mm, and $s = 0$. It is shown that the coating weight for both geometries is sensitive to the Z/D ratio and, as expected, increased with increasing Z/D. According to Gosset et al.,[7] the final coating thickness varies linearly by the jet-to-strip distances for $Z/D > 7$ for the single jet. The current study also showed the same trend for the multijet slot air knives. According to the results in Fig. 19, the coating weight for this configuration of the multislot geometry is less than the single-slot jet for $Z/D > 6$, with the largest difference being approximately 10% for $Z/D = 12$ and with no significant difference in the coating weight between the two geometries for $Z/D \leq 8$.

Effect of main jet Reynolds number

The effect of main jet Reynolds number on the final coating weight is investigated in this section. Re_m was varied between 9000 and 13,000 with $Z/D = 12$ and $Re_a = 3000$. The gas flow rate is 0.16 kg/m s, 0.19 kg/m s, and 0.24 kg/m s for $Re = 9000$, $Re = 11{,}000$, and $Re = 13{,}000$, respectively. The wall pressure gradient and wall shear stress are shown in Fig. 20. According to this Figure, the pressure gradient distribution and

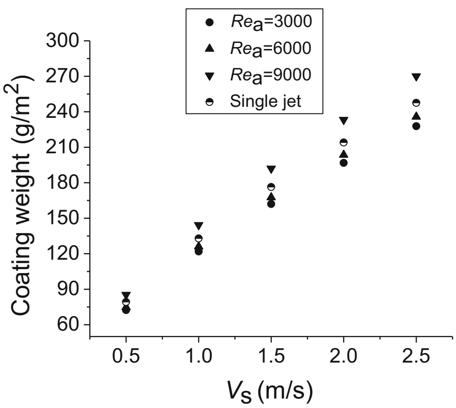

Fig. 24: Coating weight for different Re_a and V_{strip} with Z/D = 12 and Re_m = 11,000

shear stress in the vicinity of the wiping region increased with increasing Re_m. Moreover, for each Re_m the maximum pressure gradient and shear stress were larger for the modified multijet configuration vs the single-slot air-knife geometry.

Figure 21 shows the coating weight on a moving substrate for various Re_m and V_{strip}, with Re_a = 3000 and Z/D = 12, D_a = 1.5 mm D = 1.5 mm, a = 1 mm, s = 0, and θ = 8°. By increasing Re_m, the coating weight decreased for each V_{strip} and increased with increasing strip velocity. The results for the multislot design were compared with the single-slot jet coating weights. It was concluded that the coating weight for this configuration was lower for each Re_m and V_{strip} in the case of the multislot air-knife geometry.

Effect of auxiliary jet Reynolds number effect

In this section, the effect of auxiliary jet Reynolds number on the coating weight was investigated numerically, while the main slot Reynolds number was fixed at Re_m = 11,000. Figure 22 shows the wall pressure gradient and wall shear stress results for Re_a ranging between 3000 and 9000 with Re_m = 11,000 and Z/D = 12, D_a = D=1.5 mm, a = 1 mm, s = 0, and θ = 8°. It can be seen that the maximum pressure gradient was sensitive to Re_a and decreased with increasing Re_a such that the pressure gradient distribution and shear stresses were higher than those of the single jet case for $Re_a \leq 6000$.

According to Fig. 23, for high Re_a the auxiliary jet flow particles with higher velocities collide to the main jet flow and decrease its strength in the impingement region. Therefore, it decreases the wiping ability of the main jet. However, for lower Re_a the low-velocity particles of the auxiliary jet mix with the flow in the jet centerline region and increase the speed of the flow that imping on the substrate. This velocity increment is a main cause in increasing the wall shear stress and pressure gradient for this configuration in comparison with the conventional single-impinging slot jet case.

Figure 24 shows the effect of auxiliary jets Reynolds number on coating weight. It was observed that the coating weight increased with increasing Re_a for each strip velocity. It can be concluded that when the auxiliary jet Reynolds number is a fraction of the main jet Reynolds number (i.e., 25–55%), the multislot jet geometry can yield lighter coating weights.

Conclusion

A novel configuration for a multislot air knife which can be applicable for the continuous hot-dip galvanizing process as an alternative for the conventional single-slot jet was investigated numerically.

Wall pressure and wall shear stress results from the numerical simulations were used as boundary conditions in the analytical solution of the liquid film thickness in order to estimate the final coating weight on a moving substrate. In the current study, the sensitivity of the wall pressure distribution to air-knife geometry changes was investigated and a modified arrangement for the multislot jet configuration was obtained based on the CFD results. The parametric study showed that for obtaining lower coating weights, the arrangement for the multislot air knife should be in a way that the main and auxiliary jet centerlines coincide at a same point on the impingement wall. Also by decreasing the distance between the main jet and auxiliary jets and auxiliary jet width, lower coating weight can be obtained. In the next step, the effects of jet-to-wall distance, auxiliary jet Reynolds number, strip velocity, and main jet Reynolds number on the coating thickness were investigated by numerical simulations of the modified multislot air-knife design and compared to the traditional single jet geometry. It was observed that for $Z/D \geq 8$, a thinner coating thickness for higher strip velocities can be achieved by the modified multislot air knife, particularly when the auxiliary jet Reynolds number was set as a fraction of the main jet Reynolds number. Also by increasing the main jet Reynolds number, multislot air knife showed better results in terms of coating thickness reduction compared to the conventional single-slot air knife.

Acknowledgments The authors acknowledge the financial support of the International Zinc Organization Galvanized Autobody Partnership members under Project ZCO-56: Improving Coating Weight Efficiency.

References

1. Marder, AR, "Metallurgy of Zinc-Coated Steel." *Prog. Mater. Sci.*, **45** 191–271 (2000)

2. Thornton, JA, Graff, HF, "'An Analytical Description of the Jet' Finishing Process for Hot-Dip Metallic Coatings on Strip." *Metall. Trans. B*, **7** 607–618 (1976)
3. Tuck, EO, "Continuous Coating with Gravity and Jet Stripping." *Phys. Fluids*, **26** 2352 (1983)
4. Ellen, CH, Tu, CV, "An Analysis of Jet Stripping of Molten Metallic Coatings." *Eight Australas. Fluid Mech. Conf.*, **106** 399–404 (1983)
5. Myrillas, KP, Rambauda, JM, Mataigneb, P, Gardinb, S, Vincentc, JM Buchlina, "Numerical Modeling of Gas-Jet Wiping Process." *Chem. Eng. Process. Process Intensif.*, **68** 26–31 (2013)
6. Tu, CV, Wood, DH, "Wall Pressure and Shear Stress Measurements." *Exp. Therm. Fluid Sci.*, **13** 364–373 (1996)
7. Gosset, A, Rambaud, P, Castellano, L, Dubois, M, Buchlin, JM, "Modeling of Gas-Jet Wiping at Small Standoff Distances," in *6th European Coating Symposium* (2005)
8. Guo, Y, Wood, DH, "Measurements in the Vicinity of a Stagnation Point." *Exp. Therm. Fluid Sci.*, **25** 605–614 (2002)
9. Naphade, P, Mukhopadhyay, A, Chakrabarti, S, "Mathematical Modelling of Jet Finishing Process for Hot-Dip Zinc Coatings on Steel Strip." *ISIJ Int.*, **45** 209–213 (2005)
10. Elsaadawy, EA, Balthazaar, AKS, McDermid, JR, Hrymak, AN, "Coating Weight Model for the Continuous Hot-Dip Galvanizing Process." *Metall. Mater. Trans. B Process Metall. Mater. Process. Sci.*, **38** 413–424 (2007)
11. Lacanette, D, Gosset, A, Vincent, S, Buchlin, JM, Arquis, E, "Macroscopic Analysis of Gas-Jet Wiping: Numerical Simulation and Experimental Approach." *Phys. Fluids,* **18** 1–15 (2006)
12. Dubois, M, "Review on Wiping: A Key Process Limiting CGL Productivity," in *Galvatech 2011 Conference Proceedings: HDG Process Technologies,* 1847–1859 (2011)
13. Kim, GY, Park, HD, Lee, DE, Chung, WC, "Gas Wiping Apparatus Having Multiple Nozzles." US Patent 20100031879 (2008)
14. Launder, BE, Sharma, BI, "Application of the Energy Dissipation Model of Turbulence to the Calculation of Flow Near a Spinning Disc." *Lett. Heat Mass Transf.,* 131–138 (1974)
15. Alibeigi, S, Mcdermid JR, Ziada, S, Goodwin, FE, "Effect of Air Knife Geometry on Coating Weight Control in the Continuous Galvanizing Line," in *Galvatech 2013 Conference Proceedings: HDG Process Technologies,* 437–440 (2013)
16. Ritcey, A, Mcdermid, JR, Ziada, S, "Wall Shear Stress Under an Impinging Planar Jet Using the Razor Blade Technique," in *ICFMFA 2015:17th International Conf. Fluid Mechanics and Flow Analysis* (2015)